



0D (MoS_2)/2D ($\text{g-C}_3\text{N}_4$) heterojunctions in Z-scheme for enhanced photocatalytic and electrochemical hydrogen evolution

Yazi Liu^a, Huayang Zhang^a, Jun Ke^b, Jinqiang Zhang^c, Wenjie Tian^a, Xinyuan Xu^a, Xiaoguang Duan^a, Hongqi Sun^{c,*}, Moses O Tade^a, Shaobin Wang^{a,*}

^a Department of Chemical Engineering, Curtin University, GPO Box U1987, Perth, WA, 6845, Australia

^b School of Chemistry and Environmental Engineering, Wuhan Institute of Technology, Wuhan, 430073, China

^c School of Engineering, Edith Cowan University, Joondalup, WA, 6027, Australia



ARTICLE INFO

Keywords:

MoS_2 QDs
Z-scheme
Photocatalysis
Hydrogen evolution reaction (HER)
 $\text{g-C}_3\text{N}_4$

ABSTRACT

MoS_2 quantum dots (MSQDs) with high and stable dispersion in water were prepared via a facile one-pot hydrothermal process. The MSQDs were then applied to decorate graphitic carbon nitride ($\text{g-C}_3\text{N}_4$, CN) nanosheets to obtain modified $\text{g-C}_3\text{N}_4$ photocatalysts (MSQD-CN). Compared to pristine $\text{g-C}_3\text{N}_4$, the hybrid photocatalysts showed a slight red shift and stronger light absorption with remarkably improved photocatalytic activity in water splitting to generate hydrogen. The hydrogen-evolution rate over 0.2 wt% MSQD-CN increased by 1.3 and 8.1 times as high as that of 0.2 wt% Pt-CN and $\text{g-C}_3\text{N}_4$, respectively. With deposition of 2 wt% Pt as a cocatalyst, 5 wt% MSQD-CN exhibited the highest photocatalytic efficiency with an average hydrogen evolution reaction (HER) rate of $577 \mu\text{mol h}^{-1} \text{g}^{-1}$. Photoluminescence spectra (PL) and photoelectrochemical measurements inferred that MSQDs introduction drastically promoted the electron transfer for more efficient separation of charge carriers, which could lower HER overpotential barriers and enhance the electrical conductivity. In addition, the well-matched band potentials of the MSQD-CN hybrid with an intimate contact interface of p-n heterojunction also inhibited the recombination of photo-generated carriers, leading to enhanced photocatalytic HER performance. A direct Z-scheme charge transfer mechanism of the MSQD-CN hybrid was proposed to further elaborate the synergistic effect between MSQDs, Pt and $\text{g-C}_3\text{N}_4$. This work underlines the importance of heterojunction interface and presents a feasible protocol for rational construction of $\text{g-C}_3\text{N}_4$ based photocatalysts for various photocatalytic applications.

1. Introduction

Energy crisis and environmental problems have always been considered as challenging and critical issues over the past decades. Solar energy conversion into chemical energies by photocatalysis has emerged as a sustainable and efficient route. Hydrogen, as an ultimate clean energy with a much higher fuel value (143 kJ/g), is considered as an ideal candidate to replace fossil fuels in the future with wide applications in chemical industries [1]. Since Fujishima and Honda reported a photoelectrochemical hydrogen evolution process from water in 1972 [2], photocatalytic H_2 evolution over earth-abundant semiconductors combined with co-catalysts for water splitting has received considerable attention [3–5]. This shows more significances to the environmental remediation by photocatalytic process [6,7]. In practice, stable and highly efficient photocatalysts are of vital importance to the production of H_2 . Tremendous efforts have thus been focused on the development of effective surface junctions between semiconductors and

co-catalysts with a matched band structure and electron affinity, which could optimize light capture capacity and increase the charge separation to achieve overall enhanced photocatalytic performance [8].

As a metal-free semiconductor, graphitic carbon nitride ($\text{g-C}_3\text{N}_4$) has attracted much attention because of its layered graphite-like structure, suitable electronic structure for water redox catalysis as well as its simple synthesis from earth abundant elements and chemical stability [9,10]. However, pristine $\text{g-C}_3\text{N}_4$ has a relatively narrow light response range with bandgap energy at 2.7 eV [11], suffering from the fast recombination of photo-generated electron/hole pairs. Moreover, it is also restricted by low electrocatalytic activity, severely detrimental to the water splitting process. Integration of a co-catalyst, such as platinum or other noble metals, helps promote the charge separation with a prolonged lifetime for electrons to transfer over the surface, as well as to lower the overpotentials for H_2 evolution with an improved electrical conductivity [12].

Recent studies show that molybdenum sulfide (MoS_2) stands out to

* Corresponding authors.

E-mail addresses: h.sun@ecu.edu.au (H. Sun), Shaobin.wang@curtin.edu.au (S. Wang).

be a promising catalyst for hydrogen-evolution reaction (HER) with a satisfactory electrocatalytic activity originated from its unique structure [13–15]. MoS₂ has a similar layered structure to g-C₃N₄, which could achieve better lattice matching and promote the growth of MoS₂ slabs on the surface of g-C₃N₄ [16]. Moreover, the unsaturated atoms of both Mo and S at the edges will foster a favorable edge activity during the catalytic process [17]. Serving as an efficient co-catalyst, MoS₂ has already exhibited a promoting effect in photocatalytic H₂ evolution [18–21]. So far, most of MoS₂ was fabricated in 2D nanosheets to construct a hybrid with thin-layered nanojunctions [22–25]. Few studies, however, have been reported focusing on the fabrication and application of MoS₂ quantum dots (MoS₂ QDs) on g-C₃N₄. With more exposed edges as catalytically active sites than MoS₂ sheets, MoS₂ QDs appear to be a more favorable candidate as the co-catalyst in photocatalytic HER.

Herein, water-dispersible MoS₂ QDs were synthesized via a facile one-pot hydrothermal process and were then used to decorate g-C₃N₄ nanosheets by a simple impregnation method. The prepared MoS₂ QDs/g-C₃N₄ (MSQD-CN) composites showed remarkably enhanced photocatalytic H₂ evolution activities compared to pristine g-C₃N₄ and Pt/g-C₃N₄. The effect of MoS₂ QDs content on H₂ evolution rate was comprehensively studied, confirming the formation of a p-n heterojunction interface. In addition, a possible mechanism for photocatalytic H₂ evolution process over MSQD-CN composites was proposed, providing insights into designing organic-inorganic hybrid photocatalysts.

2. Experimental section

2.1. Synthesis of photocatalysts

Urea (AR) was purchased from Chem-Supply, Australia. Ammonium molybdate (99.98%), N-acetyl-L-cysteine (NAC, ≥ 99%), thiourea (≥ 99.0%), chloroplatinic acid hexahydrate (≥ 37.5% Pt basis), ethanol, methanol and acetone were supplied by Sigma-Aldrich, Australia. All reagents were used directly without any further purification.

The overall formation process of MSQD-CN composites is depicted in **Scheme 1** and more detailed information is given as follows.

Metal-free g-C₃N₄ powders were synthesized via the following procedure: 10 g of urea was placed in a furnace, heated to 550 °C at a rate of 15 °C min⁻¹ and kept at 550 °C for 4 h in air.

Water soluble MoS₂ QDs were prepared by a facile hydrothermal approach [26] with minor revision. Ammonium molybdate (4.25×10^{-3} M) and N-acetyl-L-cysteine (10.2×10^{-3} M) were mixed in 40 mL ultrapure water in an ice-water bath and stirred for a while. Then thiourea (8.5×10^{-3} M) was dissolved in the above solution with further stirring for 1 h under N₂ protection. The mixture was subsequently transferred into a 100-mL Teflon-lined stainless steel autoclave

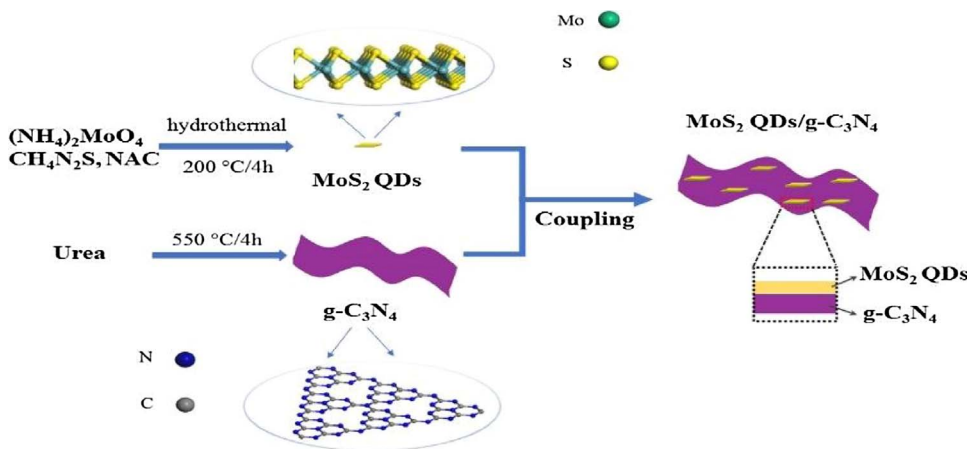
which was already de-aired with N₂ flow and kept at 200 °C for 4 h to get a high yield of MoS₂ QDs without any black sediments. After centrifuge at 13,000 rpm for 20 min, the QDs were washed with ethanol and deionized (DI) water. Finally, the QDs were transferred and dispersed in 20 mL DI water, which was able to maintain in a long-term homogeneous phase.

For synthesis of MSQD-CN, certain amounts of MoS₂ QDs solutions were sonicated for 30 min to achieve complete dispersion of the MoS₂ QDs. The as-synthesized g-C₃N₄ (0.1 g) was milled into fine powder and added to the above solution, followed by ultrasonication for 1 h. Then 10 mL acetone was added to the solution to make MoS₂ QDs deposit onto the surface of g-C₃N₄ with vigorous stirring for 24 h. After that, the precipitates were collected by centrifugation, washed with ethanol and distilled water successively, and dried at 80 °C overnight. The samples were further heated under N₂ flow at 300 °C for 1 h and noted as x wt% MSQD-CN, where x = 0, 0.2, 2.5, 5, and 7.5, respectively, representing different weight percentages of MoS₂ QDs at 0, 0.2, 2.5, 5, and 7.5 wt%. For comparison, one sample of 5 wt% MSQD-CN was synthesized following the same procedures except for the final heat treatment under N₂ flow at 120 °C for 1 h and noted as 5 wt% MSQD-CN-120 °C.

Moreover, MoS₂ nanosheets were prepared based on a previous report [19]. Ammonium molybdate (32.2 mg) and thiourea (25.12 mg) were dissolved in 40 mL distilled water followed by vigorous stirring for 1 h. Next, the homogeneous solution was transferred into a 100 mL Teflon-lined autoclave and maintained at 210 °C for 24 h. After centrifugation, the black precipitate was collected and washed with distilled ethanol and water successively, followed by drying at 80 °C. The assembly of MoS₂ nanosheets on g-C₃N₄ was achieved following the same route as 5 wt% MSQD-CN, and noted as 5 wt% MSNS-CN. Pt co-catalyst at 2.0 wt% was loaded by dissolving H₂PtCl₆ into the suspension directly, followed by ultrasonication for 10 min.

2.2. Characterization techniques

Powder X-ray diffraction (XRD) patterns were obtained on an Empyrean multipurpose research diffractometer (Panalytical Empyrean XRD) utilizing Cu K α radiation ($\lambda = 1.5418 \text{ \AA}$) with a current of 40 mA and a voltage of 40 kV. Images of scanning electron microscopy (SEM) were recorded on a FEI Verios XHR SEM microscope. Transition electron microscopy (TEM) images and selective area electron diffraction (SAED) were received with a JEOL 2100 TEM microscope. High angle annular dark field scanning transmission electron microscopy image (HAADF-STEM) mapping was obtained under a FEI TITAN G2 (200 kV). X-ray photoelectron spectroscopy (XPS) and valence band XPS (VB XPS) were conducted on a Thermo Escalab 250 spectrometer with an Al K α X-ray. A Shirley background was first subtracted followed by component fitting using Voigt functions with a 30% Lorentzian component. Fourier transformed infrared (FTIR) spectra were collected on a



Scheme 1. Schematic illustration of a synthetic route for MSQD-CN.

PerkinElmer Spectrum Two FT-IR spectrometer. UV-vis diffuse reflectance spectra (DRS) were obtained on an Agilent Cary 100 UV-vis spectrophotometer equipped with an integrated sphere attachment. Photoluminescence (PL) spectra of the samples were measured on a Cary Eclipse Fluorescence Spectrophotometer (Agilent, US).

2.3. Photocatalytic activity evaluation

Photocatalytic H₂ production experiments were carried out in a customized airtight stainless steel cell covered by a quartz window at ambient temperature. A 300 W Xeon lamp (Newport) was used as a light source with irradiation intensity centered at 35 mW/cm² for UV light and 320 mW/cm² for visible light using a light cutoff filter ($\lambda > 420$ nm). Typically, 50 mg of photocatalyst was dispersed in an aqueous solution (120 mL) containing methanol (25% by volume). Before irradiation, the suspensions were mixed under vigorous stirring for 30 min in the dark and the reaction vessel was degassed for anaerobic conditions by purging with N₂ for 30 min. The produced H₂ was in situ analyzed by a gas chromatography (Agilent 490 Micro GC) using a thermal conductivity detector.

2.4. Photoelectrochemical measurements

Photocurrent, electrochemical impedance spectroscopy (EIS) and Mott-Schottky curve measurements were conducted on a Zennium electrochemical workstation (Zahner, Germany) in a standard three-electrode framework with a 0.05 M Na₂SO₄ (pH = 6.8) electrolyte solution, adopting a Pt wire as the counter electrode and a saturated calomel electrode (SCE) as the reference electrode. As for the photo-anode, the sample film was fabricated on fluorine-doped tin oxide (FTO) glasses, which were ultrasonically cleaned in acetone and ethanol for 20 min in sequence, then dried at 60 °C. To be specific, 10 mg of the catalyst was mixed with 500 μ L of absolute ethanol and 25 μ L of Nafion solution homogeneously. The obtained slurry was then dropped onto the pretreated FTO glass via a dip-coating method with a controlled area of 1 cm², followed by drying in air for 2 h to form a film electrode. Photocurrents were obtained using a 300 W Xenon arc lamp with light passing through an AM 1.5 G filter into an optical fiber (output I₀ = 100 mW cm⁻²).

2.5. Electrocatalytic hydrogen evolution

Electrochemical measurements were carried out at room temperature on a Zennium electrochemical station (Zahner, Germany) in a standard three-electrode system, loading the samples on a glassy carbon electrode (GCE, 5 mm in diameter) as the working electrode, an Ag/AgCl electrode as the reference and a Pt wire as the counter electrode. The electrolyte was 0.5 M H₂SO₄ purged with N₂ gas (99.999%). Specifically, the catalysts of 5 mg were dispersed in 600 μ L ethanol absolute and 50 μ L 5% Nafion via ultrasonication for 1 h to form a homogeneous ink. Then 5 μ L of the slurry was deposited on the glassy carbon electrode with a catalyst loading of 0.196 mg cm⁻². The HER performance was tested by linear sweep voltammetry (LSV) at a scan rate of 10 mV S⁻¹. All the polarization curves were obtained without the ohmic potential drop (iR) correction.

3. Results and discussion

3.1. Phase structure, morphology and composition of catalysts

Fig. 1a displays XRD patterns of MSQD-CN samples with different MoS₂ QD contents (0–7.5 wt%). Both pristine g-C₃N₄ and MSQD-CN had two apparent diffraction peaks. The one centering at 27.7° can be indexed to the stacking of the conjugated double bonds for graphitic materials as the (002) crystal plane, corresponding to an interplanar distance of g-C₃N₄ at 0.336 nm, while the weak one at 12.9° represents

the (100) plane of g-C₃N₄, corresponding to the in-planar ordering of tri-s-triazine units of 0.675 nm [27]. These results confirm the formation of g-C₃N₄ with a typical graphitic, layered structure as in the previous reports [20,28]. For bare MoS₂ QDs, the appearance of a strong (002) reflection and a weak (110) reflection confirms the presence of MoS₂ quantum dots with hexagonal 2H-MoS₂ structure of JCPDS No. 37-1492 [13]. While the other peaks could be ascribed to the reflections from the substrate of quartz glass. In contrast, no apparent peaks of MoS₂ could be observed from the MSQD-CN samples, illustrating that the g-C₃N₄ nanosheet structure maintained unchanged with MoS₂ modification, possibly due to the small amount and well dispersed MoS₂ QDs on the g-C₃N₄ surface.

The elemental composition and chemical states of 5 wt% MSQD-CN sample were investigated by XPS (Figs. 1b and 2). Fig. 1b presents the XPS survey spectrum of the composite, containing elements of C, N, O and also a small amount of Mo and S. Typical peaks could be observed at binding energies of 282.6 (C 1s), 393.4 (N 1s), 527.1 (O 1s), 226.4 (Mo 3d) and 163.7 eV (S 2p). The C 1s peak in Fig. 2a can be deconvoluted into two peaks at 288.1 and 284.6 eV. The strong one at 288.1 eV could be ascribed to sp² carbon bonded to the three nitrogen atoms in the carbon nitride lattice [28–30], and the weak one corresponds to unavoidably loaded graphitic carbon atoms [31,32]. Four asymmetrical peaks at 393.9, 395.0, 396.5 and 399.8 eV can be fitted for N 1s in Fig. 2b, which can be ascribed to C=N=C sp²-bonded N atoms in graphite-like g-C₃N₄ structure, tertiary (N-(C)3) groups, amino functional groups (C—N—H), and a typical π -excitation accordingly [27,33–35]. The observed peaks of Mo 3d at 227.6 (3d_{5/2}) and 230.7 eV (3d_{3/2}) in Fig. 2c indicate that Mo element exists predominantly as Mo⁴⁺ in the composite sample. No oxidation of Mo from Mo⁴⁺ state in the MoS₂ to Mo⁶⁺ in MoO₃ occurred. The S2p spectrum Fig. 2d gives two main peaks at 162.8 and 164.3 eV, corresponding to the S 2p_{3/2} and S 2p_{1/2}, respectively, demonstrating the existence of S²⁻ state in the composite sample [18]. The high-resolution spectra further confirmed the existence of MoS₂ QDs in the as-synthesized 5 wt% MSQD-CN sample.

The microstructure and morphology of MoS₂ QDs was revealed by transmission electron microscopy (TEM). Fig. 3a shows that the mean diameter of MoS₂ QDs particles is about 1.7 nm. According to the inset graph of particle size distribution, about 89.2% MoS₂ QDs show a particle size within the range of 1.5–2.5 nm, which are homogeneous without obvious aggregation. A typical hexagonal lattice structure with high crystallinity can be observed with ordered lattice fringe (103) from the high-resolution transmission electron microscopy (HRTEM) image in Fig. 3b, showing a lattice spacing of 0.230 nm in the inset amplified image [36]. Fig. S2 shows the typical SEM and TEM images of a light yellow fluffy powder of g-C₃N₄, exhibiting a typical layered sheet-like structure. TEM images of the 5 wt% MSQD-CN composite sample (Fig. 3c) reveal that thin and sheet-like g-C₃N₄ was decorated with crystallized MoS₂ QDs in random distribution. As shown in Fig. 3d, the lattice distance of g-C₃N₄ crystallites was measured to be 0.34 nm, corresponding to the (002) plane of hexagonal g-C₃N₄ (JCPDS 87-1526) and in conformity with the XRD results. Meanwhile, the lattice spacing of 0.59 nm (JCPDS 37-1492), corresponding to the (002) facet of MoS₂ QDs, was also observed. Thus, the MoS₂ QDs were proved to be closely attached to the g-C₃N₄ nanostructure via their (002) crystal planes with intimate interfacial contact, which might be favorable for promoting the charge separation in the electron-transfer process for photocatalytic H₂ evolution. In addition, the HAADF-STEM elemental mapping (Fig. 3e) of 5 wt% MSQD-CN sample further proves that MoS₂ QDs were immersed well into a broader g-C₃N₄ matrix with the elements of Mo and S exhibiting a low density at the same location.

3.2. Optical properties

The optical absorption properties of g-C₃N₄, MoS₂ QDs and MSQD-CN composites are shown in Figs. 4 and S3. For the MoS₂ QDs, it can be

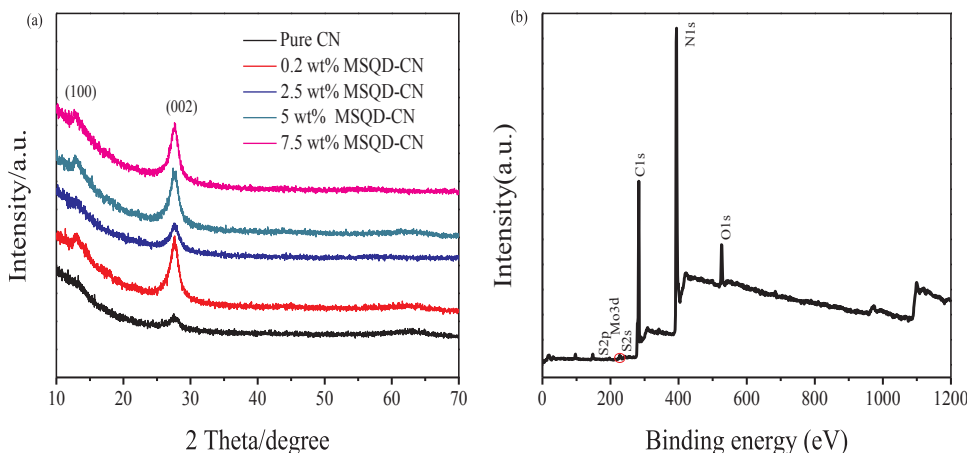


Fig. 1. (a) XRD patterns of MSQD-CN composite samples and pure $g\text{-C}_3\text{N}_4$. (b) XPS survey of 5 wt% MSQD-CN.

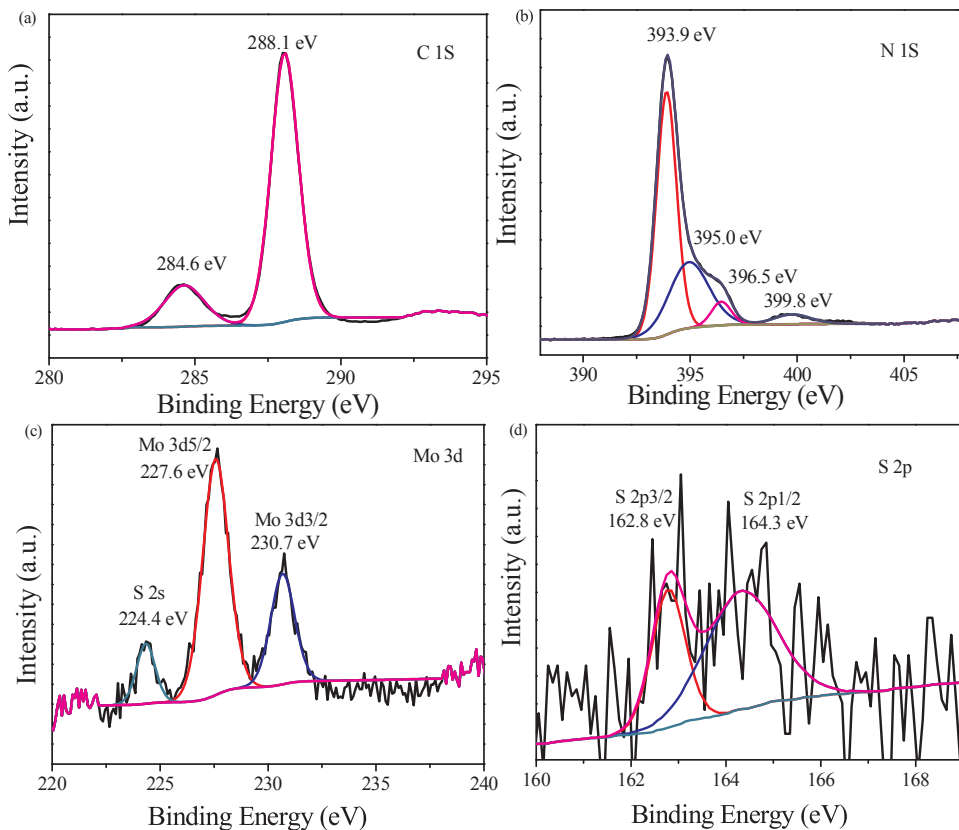


Fig. 2. (a) C 1s (b) N 1s (c) Mo 3d and (d) S 2p spectra of 5 wt% MSQD-CN.

observed from Fig. S3 that the peaks at 207 and 230 nm show excitonic features of MoS_2 quantum dots [36,37]. The peaks at 380 and 367 nm should be assigned to excitonic absorption bands due to direct band-gap transition at K point with energy split from valence band spin-orbital coupling [26]. Compared to the absorption edge of bulk MoS_2 and monolayer MoS_2 nanosheets in previous reports [19,38], a large blue-shift was observed due to the strong quantum confinement effect [39] of MoS_2 QDs as the majority of the particles are within the size of 2–5 nm. The inset image in Fig. S3 exhibits the high stability and good dispersion of MoS_2 QDs in water without noticeable agglomeration for two months. As can be seen from Fig. 4a, the steep edge at around 380 nm should be assigned to the band gap transition of $g\text{-C}_3\text{N}_4$ [40]. For the composite samples, all of their absorption edges present a slight red-shift. In addition, the introduction of MoS_2 QDs enhanced both UV and visible light absorption capacity of the composite samples. It is worth noting that 5 wt% MSQD-CN outperformed other samples, which

might lead to enhanced production of electron-hole pairs and thus a possibly higher photocatalytic activity. The band-gap energies of all the samples were estimated based on the Kubelka-Munk theory [9,40,41] following the equation of $(\alpha h\nu)^n = k(h\nu - E_g)$ (where α , ν , k and E_g represent absorption factor, light frequency, proportionality constant and band gap energy, respectively). Based on the UV-vis diffuse reflectance spectra in Figs. 4a and S3, $(\alpha h\nu)^n$ ($n = 2$ for direct-gap semiconductors and $n = 1/2$ for indirect-gap semiconductors) versus $h\nu$ was then plotted in Figs. 4b and S3 (inset) with values shown in Table S1. The decreased band-gap energy of the composite with the increasing content of MoS_2 -QDs proves that the MoS_2 QDs decoration changed the semiconductor composite properties of $g\text{-C}_3\text{N}_4$ due to mutual interaction. The direct band-gap energy for pure MoS_2 -QDs has been determined to be 3.41 eV. As for pristine $g\text{-C}_3\text{N}_4$, the band-gap value of 2.90 eV is larger than bulk $g\text{-C}_3\text{N}_4$, and much closer to $g\text{-C}_3\text{N}_4$ nanosheets according to previous reports [42–44], which proved that the

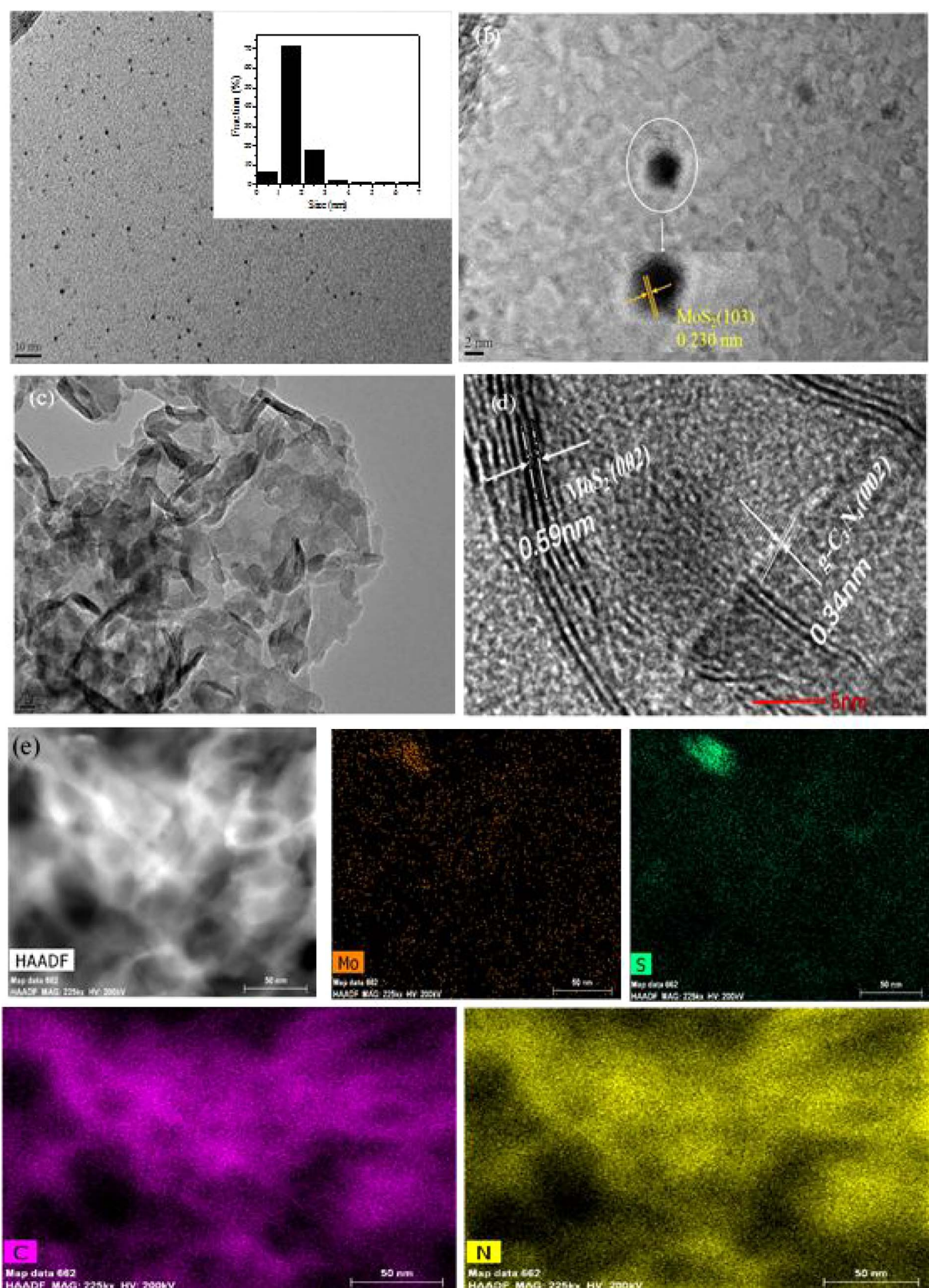
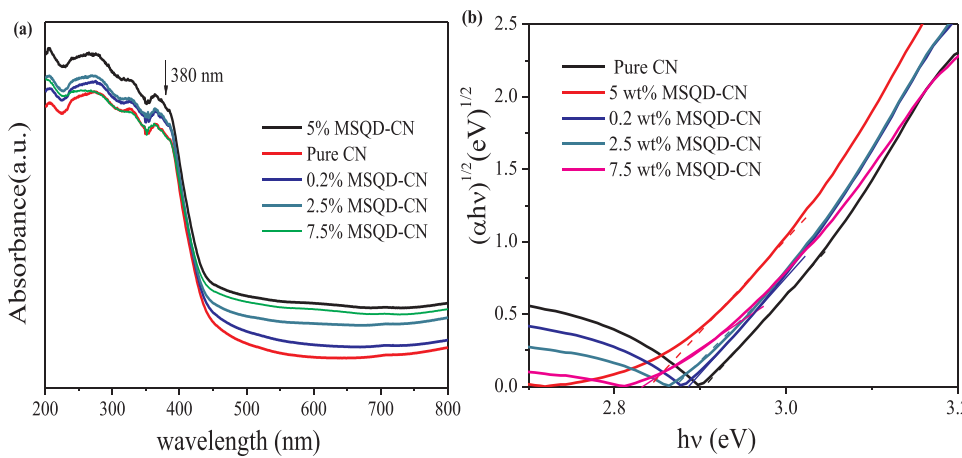


Fig. 3. TEM and HRTEM images of (a–b) MoS₂ QDs (insert shows corresponding particle size distribution); (c–d) 5 wt% MSQD-CN; (e) High angle annular dark field scanning TEM image and corresponding EDX elemental mapping of 5 wt% MSQD-CN sample.



$\text{g-C}_3\text{N}_4$ prepared in this study exhibits a thin, sheet-like structure. This enlarged band-gap energy of nanostructured semiconductor compared to its bulk counterpart is also attributed to the well-known quantum confinement effect, shifting its absolute conduction and valence band in opposite directions [45].

To investigate the charge carrier separation, transferring, and trapping in pure $\text{g-C}_3\text{N}_4$ and MSQD-CN composite samples, the photoluminescence (PL) was conducted (Fig. S4a). All the photocatalysts exhibit similar emission trends at an excitation wavelength of 325 nm at room temperature. The main emission peak centered at around 460 nm for pure $\text{g-C}_3\text{N}_4$ is attributed to the recombination of the photoexcited electron-hole pairs originating from the intrinsic HOMO-LUMO transition [27,32]. The main emission peaks of the MSQD-CN composites shift slightly to the left, compared with the spectrum of pure $\text{g-C}_3\text{N}_4$. This blue shift of fluorescence emission spectrum further confirmed the enlarged band-gap energy after introduction of MoS_2 QDs. The only exception is for the sample of 0.2 wt% MSQD-CN, which might be due to extremely low content of MoS_2 QDs. Looking into the peak intensities around 640 nm, both 5 wt% MSQD-CN and 2.5 wt% MSQD-CN show a lower PL intensity relative to $\text{g-C}_3\text{N}_4$. This observation indicated that the quantum-sized MoS_2 and its heterojunction with $\text{g-C}_3\text{N}_4$ induced efficient charge transfer at the interface, suppressing the recombination of photogenerated electrons and holes. The PL results were in agreement with UV-vis absorption behavior and the corresponding photocatalytic H_2 evolution activities shown in the next section. In addition, the PL spectra of pure MoS_2 QD were also investigated under different excitation wavelengths at room temperature (Fig. S4b). Similarly, it also shows a marked blue-shift in comparison with those of monolayer MoS_2 nanosheets [26]. With the increase of the excitation wavelength from 220 to 400 nm, a red shift of emission peaks from 440 to 800 nm was observed, while its intensity decreased noticeably over the

excitation wavelength ranging from 300 to 400 nm. This may be ascribed to the direct excitonic transitions from the K point of the Brillouin zone, the presence of polydispersity and various trap states in MoS_2 quantum dots [26,36,46–49]. The strongest emission peak occurs at the excitation wavelength of 300 nm, which should be resulted from the transition at the K point with energy split of valence band [26]. Furthermore, it was observed that the emission wavelength of the PL also depends on the particle size of the MoS_2 QDs, possibly due to the quantum size effect. Based on previous studies [48], medium-sized MoS_2 QDs (1.5–3 nm) usually emit visible light within the range of 400–700 nm, which is in accordance with the particle size measurements in TEM for the MoS_2 QDs synthesized in this paper.

3.3. Photocatalytic H_2 -production activity and stability

H_2 evolution on pure $\text{g-C}_3\text{N}_4$ and 5 wt% MSQD-CN samples annealed at different temperatures (120 and 300 °C) were tested (Fig. S5a). The photocatalytic H_2 -evolution rates of 5 wt% MSQD-CN-300 °C and 5 wt% MSQD-CN-120 °C were elevated to approximately 1.8 and 1.5 times of the pristine $\text{g-C}_3\text{N}_4$, which might be ascribed to the establishment of efficient heterojunction between $\text{g-C}_3\text{N}_4$ and MoS_2 QDs.

The photocatalytic water reduction using different amount of MoS_2 QDs decorated $\text{g-C}_3\text{N}_4$ at 300 °C were further investigated (Fig. 5). As a traditional and efficient co-catalyst, Pt is adopted to reduce the overpotential required for water splitting to H_2 evolution. Control experiments show no H_2 was detected with Pt or pure MoS_2 QDs only, indicating that Pt or MoS_2 QDs alone is not active for photocatalytic H_2 evolution. After 240 min of light irradiation, total hydrogen evolution over pure $\text{g-C}_3\text{N}_4$ reached 62.9 μmol . After impregnation with MoS_2 QDs, the photocatalytic H_2 evolution activity was significantly enhanced. The rate of H_2 evolution reached the maximum of

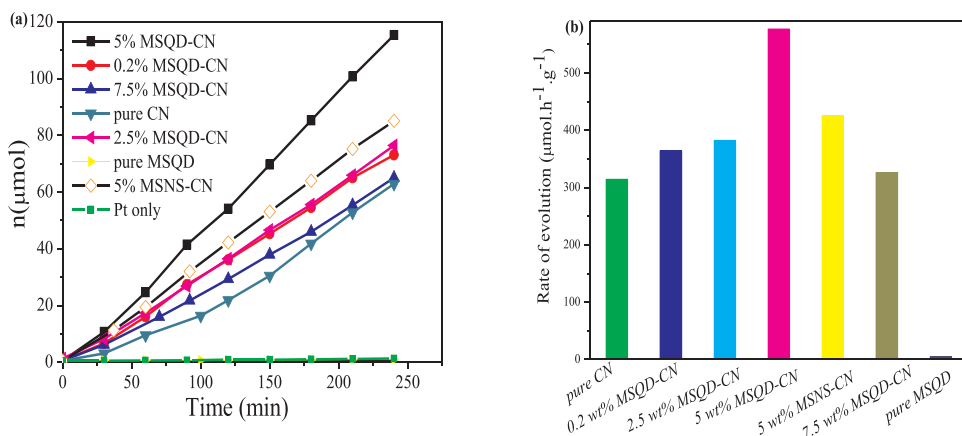


Fig. 5. (a) Photocatalytic activity for H_2 evolution and (b) average photocatalytic H_2 evolution rate over different samples under simulated solar light irradiation. (25 vol% methanol, 2.0 wt% Pt, 0.05 g catalyst in 120 mL aqueous solution).

577 $\mu\text{mol h}^{-1} \text{g}^{-1}$ at 5 wt% MoS₂ QDs, which ranks among the top photocatalytic H₂ evolution activities based on recent studies as shown in Table S2. A further increase in MoS₂ QDs loading led to a drop in the photocatalytic hydrogen evolution. It is reported that excessive loading of MoS₂ may not be favorable for photo-redox catalytic reaction due to the blocking effect to hinder the light absorption of g-C₃N₄ [50]. This hypothesis conforms to the results from UV-vis spectra. Previous reports showed that MoS₂ with thin layers could improve charge transport across the layers by shortening the path and speeding up the transportation process for photo-generated electrons to enhance photocatalytic efficiency for hydrogen generation [15,51]. Additionally, 5 wt% MSNS-CN exhibits a higher hydrogen-evolution rate than pure g-C₃N₄, but much lower than that on 5 wt% MSQD-CN. Compared with thin-layered MoS₂ nanosheet, which has been recognized as an effective HER catalyst [14,52], MoS₂ quantum dots possess a higher quantum confinement and smaller-size, providing more opportunity for their unsaturated bonds to connect with other atoms to form an intimate contact between MoS₂ and g-C₃N₄. MoS₂ QDs also boost a superior HER activity by lowering activation barriers with a high electrical conductivity [21], leading to a higher photocatalytic H₂-evolution activity.

As for visible light irradiation, it can be noticed in Fig. S5b that 5 wt % MSQD-CN exhibited a slightly better photocatalytic H₂-evolution performance than pure g-C₃N₄. After 240 min of visible light irradiation, the total hydrogen evolution over g-C₃N₄ and 5 wt% MSQD-CN reached 162.2 and 222.9 $\mu\text{mol g}^{-1}$, respectively.

In addition, it can be seen from Fig. 6a that the as-synthesized 0.2 wt % MSQD-CN without Pt deposition showed a higher activity in photocatalytic H₂ evolution than 0.2 wt% Pt-CN with an enhancement about 20%. The photocatalytic H₂ evolution was very low (only 3.29 μmol after 240 min) on g-C₃N₄ without loading any co-catalyst. An ideal co-catalyst often provides relatively low activation potentials for H₂ evolution and also promotes prompt transportation of photo-induced charge carriers, serving as the active sites for photocatalytic H₂ evolution [50]. As a noble metal, Pt is recognized as one of the best co-catalysts to promote H₂ evolution [53], but in this study the rate of H₂ evolution over 0.2 wt% Pt-CN is lower than that of 0.2 wt% MSQD-CN. This result proves that MoS₂ quantum dots could serve as an efficient co-catalyst with the potential to replace noble metals, constructing effective surface junctions with g-C₃N₄ with a structural and electronic compatibility, which is crucial for enhancing photocatalytic activity.

As mentioned above, no H₂ was detected on pure MoS₂-QDs. While the decoration of MoS₂-QDs on g-C₃N₄ was able to drastically improve the H₂ evolution from 16.45 $\mu\text{mol h}^{-1} \text{g}^{-1}$ on pure g-C₃N₄ to 132.68 $\mu\text{mol h}^{-1} \text{g}^{-1}$ on 0.2 wt% MSQD-CN in the absence of Pt. When Pt was loaded on the catalyst of 0.2 wt% MSQD-CN as an electron collector, the H₂ yield was further improved to 363.9 $\mu\text{mol h}^{-1} \text{g}^{-1}$.

The stability of 5 wt% MSQD-CN photocatalyst was further investigated in recycling photocatalytic experiments. Fig. 6b displays the H₂ evolution in a 12 h photocatalytic run with 4 h intermittence over the

sample of 5 wt% MSQD-CN. Only a slight decrease of photocatalytic H₂ evolution was detected for 5 wt% MSQD-CN composite after three recycling runs. The XRD and FT-IR profiles in Fig. S6 reveal that no apparent change occurred on 5 wt% MSQD-CN before and after the three cycles of photocatalytic H₂ evolution reactions. It is inferred that the small loss of activity might be attributed to the oxidation or corrosion of MoS₂ by photo-induced holes during the reaction process [50]. These results confirm that the MSQD-CN composites possess sufficient stability without structural change during the photocatalytic reaction process.

3.4. Photocatalytic mechanism

Photoelectrochemical properties of the catalysts were explored concerning the charge transfer and separation rates for photocatalytic mechanism. Transient photocurrents of g-C₃N₄ and 5 wt% MSQD-CN were studied (Fig. S7). Compared with g-C₃N₄, the photocurrent intensity of 5 wt% MSQD-CN decreased but exhibited a higher stability after four cycles. The photocurrent was obtained by guiding photo-induced electrons moving to external circuit. The density of photocurrent depends on many factors, such as quality of working electrode, light harvesting ability of samples, and transfer efficiency of electrons. Therefore, the measured photocurrent intensity is not closely correlated with its photocatalytic performance. To further verify the relationship between photoactivity and electrochemical properties, electrochemical impedance spectroscopy (EIS) was adopted to complement the photocurrent curves as a more convincing and powerful technique in studying the interfacial charge transport behavior and efficiency [54,55]. EIS measurements were performed and recorded in the semi-circular Nyquist diagram as shown in Fig. 7a. It is observed that the arc radius of the Nyquist plot of 5 wt% MSQD-CN is much smaller compared to that of pure g-C₃N₄ and MoS₂ quantum dots, indicating a lower charge transfer resistance with improved charge separation efficiency. This result further confirms that the decoration of MoS₂ quantum dots on g-C₃N₄ could accelerate charge separation and transportation with a much slower recombination rate of photo-generated electron/hole pairs, which is a key contributor to the enhancement of photocatalytic H₂ production and also in agreement with the above PL results.

To gain further insights into the intrinsic properties of the heterojunction between MoS₂ QDs and g-C₃N₄, Mott-Schottky (M-S) measurements were conducted to determine the flat band potential values as well as electronic band structure shifts (Fig. 7b–d), which can be estimated from the plots based on Eq. (1),

$$1/C^2 = (2/\epsilon_r \epsilon_0 e N_d A^2) [(V - V_{fb}) - kT/e] \quad (1)$$

where V_{fb} (the flat band potential) can be obtained from the intercept of the plot tangents on X-axis when plotting $1/C^2$ (C is the specific capacity) versus V (V is the applied potential). The positive slope of the tangent lines in Fig. 7b indicates that g-C₃N₄ is an n-type

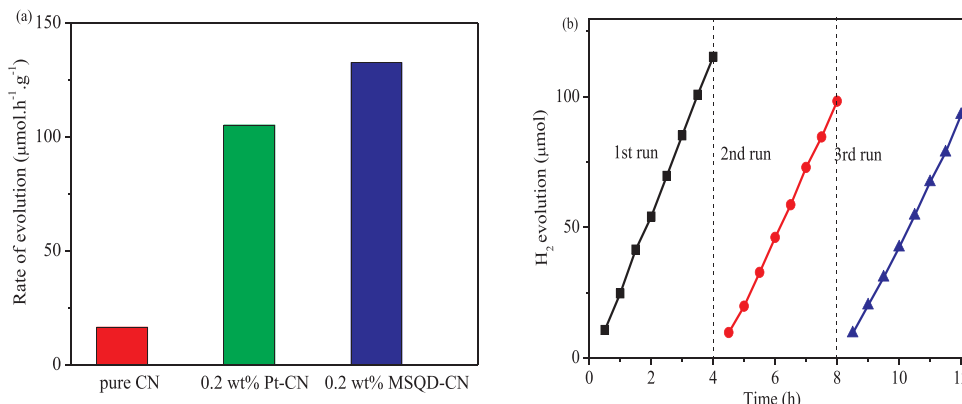


Fig. 6. (a) Rate of H₂ production over CN loaded with different co-catalysts and (b) Cycle runs for the photocatalytic H₂ production on 5 wt% MSQD-CN (25 vol% methanol, 0.05 g catalyst in 120 mL aqueous solution).

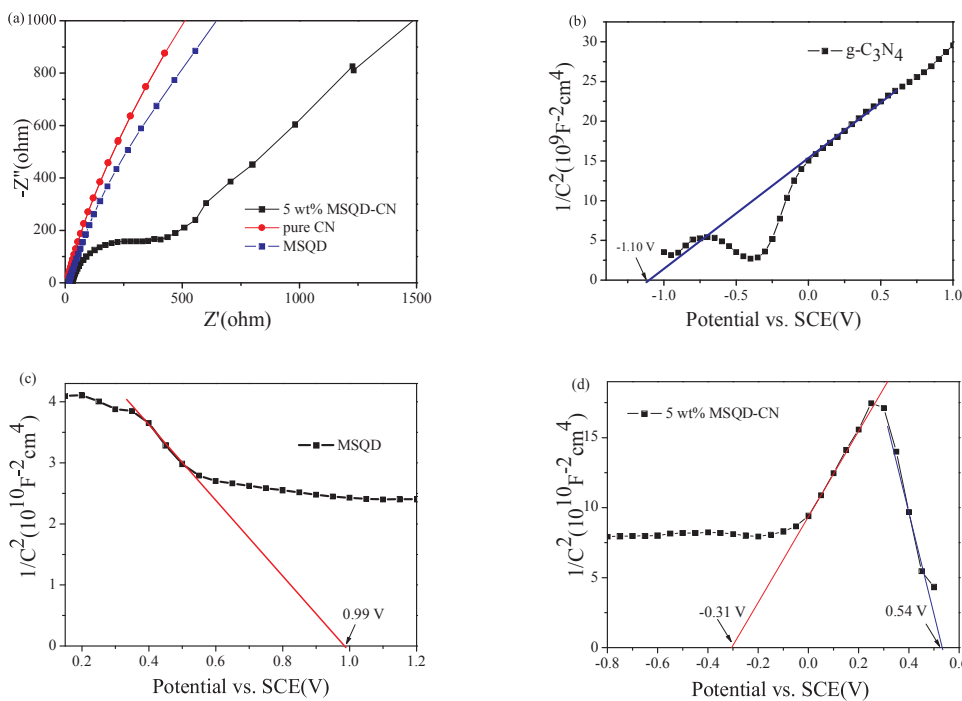


Fig. 7. Nyquist plots of electrochemical impedance spectroscopy (EIS) with different electrodes in dark (a); Mott–Schottky curves collected on $g\text{-C}_3\text{N}_4$ (b), MoS_2 QDs (c) and 5 wt% MSQD-CN (d).

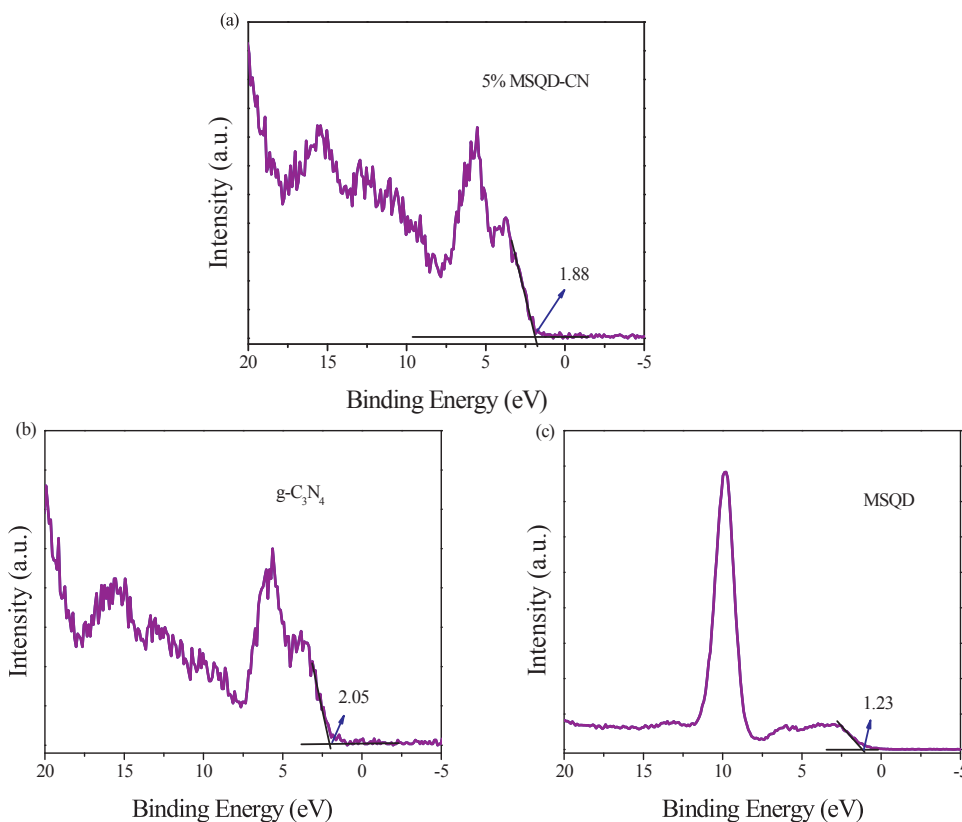
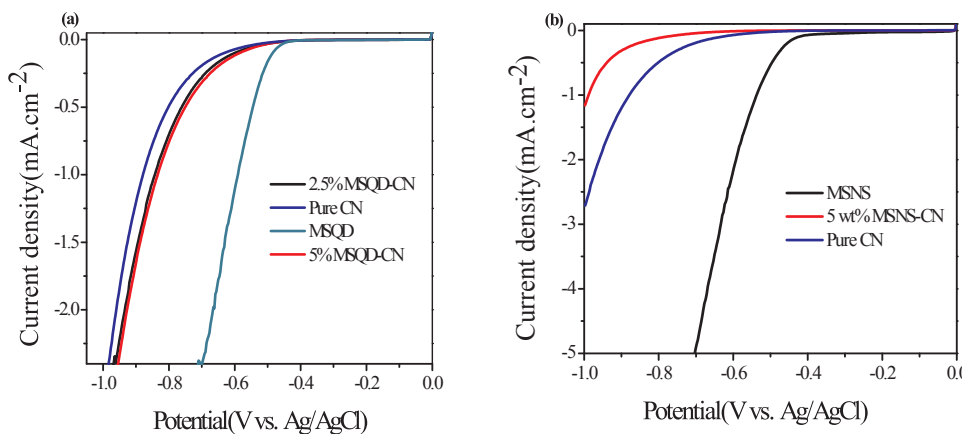


Fig. 8. VB XPS spectra of (a) 5 wt% MSQD-CN, (b) $g\text{-C}_3\text{N}_4$ and (c) MoS_2 QDs.

semiconductor, for which the lowest potential of conduction band (CB) can be extremely close to its flat-band potential. While for MoS_2 QDs, a typical p-type semiconductor was observed with a negative slope of the plot in Fig. 7c, whose highest potential of valence band (VB) could be estimated from its flat-band potential accordingly. The flat band potentials of n-type $g\text{-C}_3\text{N}_4$ and p-type MoS_2 QDs were calculated to be -1.10 V vs. SCE (-0.86 V vs. NHE) and 0.99 V vs. SCE (1.23 V vs. NHE), respectively [56]. It is worth noting that an inverted ‘V-shape’ is

present in Fig. 7d, confirming that a p-n heterojunction forms at the interface between $g\text{-C}_3\text{N}_4$ and MoS_2 QDs with distinct electronic behavior [56]. Therefore, an internal electrical field (E_{internal}) will be formed with a direction from n-type $g\text{-C}_3\text{N}_4$ to p-type MoS_2 , leading to much more efficient charge separation of the photo-generated electrons and holes. To better elucidate the photocatalytic mechanism and draw the schematic diagram of energy band structure, the exact CB and VB positions for $g\text{-C}_3\text{N}_4$, MoS_2 QDs and 5 wt% MSQD-CN were also verified



by valence band (VB) XPS measurement, which could give detailed information related to the total density of states (DOS) of the valence band of the samples [57–59]. The results are presented in Fig. 8. As shown, the maximum VB energies of 5 wt% MSQD-CN, g-C₃N₄ and MoS₂ QDs were calculated to be at 1.88 eV, 2.05 eV and 1.23 eV, respectively. Combined with band gap energy of 2.90 eV for g-C₃N₄ in Table S1, the minimum conduction band (CB) energy could be obtained to be at about -0.85 eV. Both of the results conform well to the flat band potential values estimated in Fig. 7.

To further identify the roles of MoS₂ QDs as a co-catalyst in promoting H₂ evolution activity during the photocatalytic process, electrochemical polarization curves were obtained in a typical three electrode cell. Fig. 9a depicts the electrocatalytic H₂-evolution activity for g-C₃N₄, MoS₂ QDs and different MSQD-CNs, showing an obvious cathodic current in the range of -0.4–-1.0 V (versus Ag/AgCl) with respect to H₂ evolution reaction (HER). Clearly, MoS₂ QDs exhibited the lowest onset potential for H₂ evolution (only -0.44 V vs Ag/AgCl, obtained via the intercept of the plot tangents on horizontal axis) with the highest HER performance, while pure g-C₃N₄ showed the lowest HER activity with an onset potential of -0.54 V vs Ag/AgCl. After introduction of MoS₂ QDs, MSQD-CN sample exhibited proper onset potentials for H₂ evolution, revealing that the MoS₂ QDs plays a key role in decreasing the onset potential and improving electrocatalytic efficiency by acting as an active site. Consequently, the HER performance of MSQD-CN was enhanced with the lowering of activation barriers and

improved kinetics for H₂ evolution. In addition, 5 wt% MSQD-CN sample (-0.47 V vs Ag/AgCl) outperforms 2.5 wt% MSQD-CN sample (-0.51 V vs Ag/AgCl) with a lower onset potential, which agrees well with the tests of photocatalytic H₂ evolution activity. Meanwhile, Fig. 9b shows the electrocatalytic H₂-evolution activities of g-C₃N₄, as-synthesized MoS₂ nanosheets and 5 wt% MSNS-CN. Unlike the MSQD-CN, after introduction of MoS₂ nanosheets, the HER performance of 5 wt% MSNS-CN dropped significantly with an even higher onset potential. These results indicate that effective and intimate contact at the nanojunction of MoS₂ and g-C₃N₄ is of vital importance to lower activation barriers as well as electron transport, which may account for the inferior photocatalytic H₂ production on 5 wt% MSNS-CN to 5 wt% MSQD-CN.

Based on the results and discussions above, it is concluded that the improved photocatalytic H₂-evolution activity of the MSQD-CN composites could be ascribed to the enhancement of light absorption capacity as well as much more efficient separation of photogenerated electron/hole pairs. It was reported that the distance between electrons and holes is crucial to the inhibition of efficient recombination and prolonged lifetime of charge carriers. As a co-catalyst, MoS₂ QDs co-operating with g-C₃N₄ could increase light absorption and lower the activation barriers for H₂ evolution, facilitating faster electron transfer across the interface with improved photocatalytic activity. However, thick layered MoS₂ nanosheet leads to the light blocking effect, not favorable for light utilization by g-C₃N₄. Optimal loading of 5 wt%

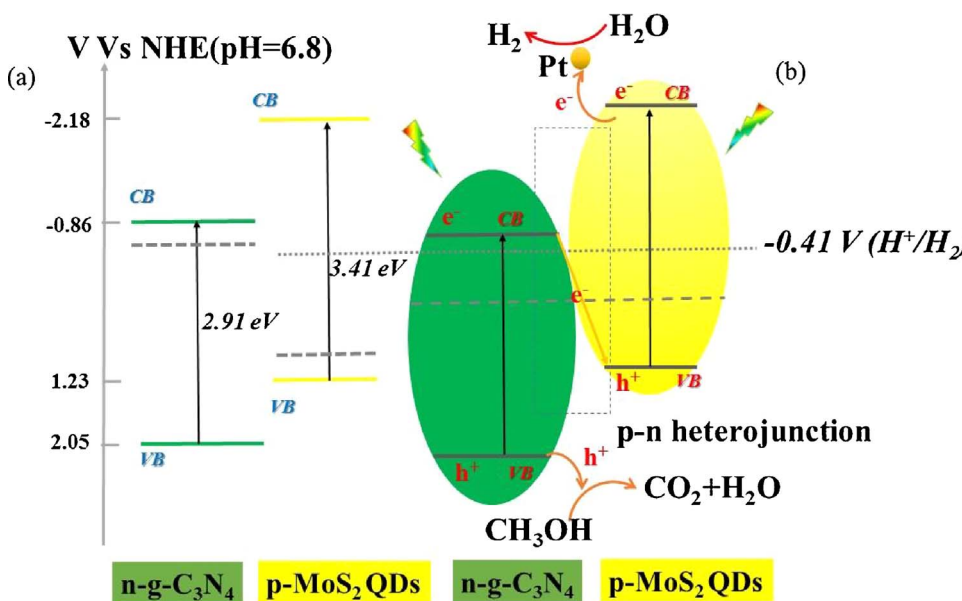


Fig. 10. Schematic diagram of energy band structure and proposed mechanism (a) before contact; (b) after formation of g-C₃N₄ and MoS₂ QDs p-n heterojunction.

MoS₂ QDs achieves the superior balance between light harvesting in g-C₃N₄ and charge transfer between g-C₃N₄ and MoS₂ QDs.

The energy band structure and photo-generated charge transfer scheme are illustrated in Fig. 10. It is shown that the conduction band of MSQD-CN is properly positioned above the reduction level of H₂, which allows electrons to transfer for water reduction. From the band gap structures of MoS₂ QDs and g-C₃N₄, traditional heterojunction-transfer mechanism [24,60–62] may not well interpret the results illustrated in Fig. 10. In the traditional heterojunction-transfer mechanism, the photoexcited electrons will inevitably be transferred from the CB of MoS₂ QDs (−2.18 eV) to the CB of g-C₃N₄ (−0.86 eV), leading to the drop in electron reduction potential. As such, the electrons accumulated on the CB of g-C₃N₄ will experience difficulty in reducing H⁺ into H₂, especially in case of no Pt as a cocatalyst (Fig. 6a). According to recent reports [56,63–65], the enhanced photocatalytic H₂-evolution activity could be properly explained following the PS-PS system of Z-scheme charge transfer mechanism for the MSQD-CN system. Under solar light irradiation, both of the electrons from the VB of MoS₂ QDs and g-C₃N₄ will be excited to the CB of MoS₂ QDs and g-C₃N₄ correspondingly. Owing to the short electron-migration distance between MoS₂ QDs and g-C₃N₄ nanosheets, the photogenerated electrons from CB of g-C₃N₄ will combine rapidly with the photogenerated holes from VB of MoS₂ QDs at the formed ohmic contact in the solid-solid interface. Therefore, more oxidative holes and reductive electrons will be retained in VB of g-C₃N₄ and CB of MoS₂ QDs separately, leading to the enhancement of overall photocatalytic performance. Meanwhile, after coupling g-C₃N₄ and MoS₂ QDs, the internal electrical field was formed at the interfacial phases as a p-n heterojunction, promoting much more efficient charge separation of e[−]/h⁺ pairs [41]. MoS₂ QDs possess a more negative E_{CB} with strong reducibility as an electron collector with unsaturated active S atoms at the exposed edges and will easily reduce the bonded H⁺ to H₂ [66]. Moreover, some electrons in the CB of MoS₂ QDs will also transfer to metallic Pt and then get involved in H₂ evolution. At this point, MoS₂ QDs boosts the H₂-evolution surface active sites over g-C₃N₄ nanosheets owing to its much lower electrocatalytic H₂-evolution overpotentials [21]. In a word, 5 wt% MSQD-CN exhibits an excellent photocatalytic H₂-evolution activity with enhanced light absorption ability, a smaller onset potential with a higher electrical conductivity and a stronger reductive capability. In addition, it is plausible to explain why the 5 wt% MSQD-CN sample shows a slightly higher photocatalytic H₂-evolution activity than pure g-C₃N₄ under visible light only. Under the visible light irradiation ($\lambda > 420$ nm), MoS₂ QDs with a large band gap energy of 3.41 eV can hardly get photoexcited, while only g-C₃N₄ with a smaller band gap energy can respond to visible light with photo-generated electrons and holes in the CB and VB of g-C₃N₄ respectively. As a result, the recombination without fast separation via Z-scheme charge transfer mechanism would thus occur.

4. Conclusions

In summary, uniform water-soluble MoS₂ QDs with sizes of 2–5 nm were prepared via a facile one-pot hydrothermal process and were employed to modify g-C₃N₄ nanosheets for MoS₂ QDs/g-C₃N₄ photocatalysts with high photocatalytic and electrochemical H₂ evolution activities. The introduction of MoS₂ QDs results in a red shift and stronger light absorption capability in comparison with pure g-C₃N₄. Owing to quantum confinement effect, MoS₂ QDs facilitate a faster electron transfer and efficiently prevent the charge recombination via lowering overpotential barriers and charge-transfer resistance. In addition, the well-matched band-structure of MSQD-CN composite conforms to Z-scheme charge transfer mechanism with a higher reductive capability, leading to the enhancement of photocatalytic H₂ evolution activity. The highest photocatalytic H₂ evolution activity was found on 5 wt% MSQD-CN, superior to the as-synthesized 5 wt% MSNS-CN. This study provides a novel strategy for designing p-n heterostructured

photocatalysts for solar hydrogen production in the future.

Acknowledgments

This work was financially supported by the Australian Research Council (DP150103026). The authors acknowledge the technical supports from the Centre for Microscopy, Characterization and Analysis, The University of Western Australia; Electron Microscope Facility, Curtin University; as well as the X-ray Surface Analysis Facility, Curtin University, funded by the Australian Research Council LIEF Grant (LE120100026).

Appendix A. Supplementary data

Supplementary material related to this article can be found, in the online version, at doi:<https://doi.org/10.1016/j.apcatb.2018.01.067>.

References

- [1] N.S. Lewis, D.G. Nocera, PNAS 103 (2006) 15729–15735.
- [2] A. Fujishima, Nature 238 (1972) 37–38.
- [3] J. Liu, Y. Liu, N. Liu, Y. Han, X. Zhang, H. Huang, Y. Lifshitz, S.-T. Lee, J. Zhong, Z. Kang, Science 347 (2015) 970–974.
- [4] Y. Li, T. Takata, D. Cha, K. Takanabe, T. Minegishi, J. Kubota, K. Domen, Adv. Mater. 25 (2013) 125–131.
- [5] A. Kudo, Y. Miseki, Chem. Soc. Rev. 38 (2009) 253–278.
- [6] G.L. Zhou, H.Q. Sun, S.B. Wang, H.M. Ang, M.O. Tade, Sep. Purif. Technol. 80 (2011) 626–634.
- [7] H.Q. Sun, Y. Bai, H.J. Liu, W.Q. Jin, N.P. Xu, G.J. Chen, B.Q. Xu, J. Phys. Chem. C 112 (2008) 13304–13309.
- [8] M.G. Walter, E.L. Warren, J.R. McKone, S.W. Boettcher, Q. Mi, E.A. Santori, N.S. Lewis, Chem. Rev. 110 (2010) 6446–6473.
- [9] H. Sun, G. Zhou, Y. Wang, A. Suvorova, S. Wang, ACS Appl. Mater. Interfaces 6 (2014) 16745–16754.
- [10] L. Zhou, H.Y. Zhang, H.Q. Sun, S.M. Liu, M.O. Tade, S.B. Wang, W.Q. Jin, Catal. Sci. Technol. 6 (2016) 7002–7023.
- [11] X. Wang, K. Maeda, A. Thomas, K. Takanabe, G. Xin, J.M. Carlsson, K. Domen, M. Antonietti, Nat. Mater. 8 (2008) 76.
- [12] K. Maeda, K. Teramura, D. Lu, T. Takata, N. Saito, Y. Inoue, K. Domen, Nature 440 (2006) 295–295.
- [13] J. Xie, H. Zhang, S. Li, R. Wang, X. Sun, M. Zhou, J. Zhou, X.W. Lou, Y. Xie, Adv. Mater. 25 (2013) 5807–5813.
- [14] Y. Hou, Z. Wen, S. Cui, X. Guo, J. Chen, Adv. Mater. 25 (2013) 6291–6297.
- [15] Y. Yang, H. Fei, G. Ruan, C. Xiang, J.M. Tour, Adv. Mater. 26 (2014) 8163–8168.
- [16] Y.J. Hong, T. Fukui, ACS Nano 5 (2011) 7576–7584.
- [17] L.S. Byskov, J.K. Nørskov, B.S. Clausen, H. Topsøe, J. Catal. 187 (1999) 109–122.
- [18] Q. Xiang, J. Yu, M. Jaroniec, J. Am. Chem. Soc. 134 (2012) 6575–6578.
- [19] W. Zhou, Z. Yin, Y. Du, X. Huang, Z. Zeng, Z. Fan, H. Liu, J. Wang, H. Zhang, Small 9 (2013) 140–147.
- [20] J. Li, E. Liu, Y. Ma, X. Hu, J. Wan, L. Sun, J. Fan, Appl. Surf. Sci. 364 (2016) 694–702.
- [21] F. Li, J. Li, Z. Cao, X. Lin, X. Li, Y. Fang, X. An, Y. Fu, J. Jin, R. Li, J. Mater. Chem. A 3 (2015) 21772–21778.
- [22] H. Xu, J. Yi, X. She, Q. Liu, L. Song, S. Chen, Y. Yang, Y. Song, R. Vajtai, J. Lou, H. Li, S. Yuan, J. Wu, P.M. Ajayan, Appl. Catal. B 220 (2018) 379–385.
- [23] W. Fu, H. He, Z. Zhang, C. Wu, X. Wang, H. Wang, Q. Zeng, L. Sun, X. Wang, J. Zhou, Q. Fu, P. Yu, Z. Shen, C. Jin, B.I. Yakobson, Z. Liu, Nano Energy 27 (2016) 44–50.
- [24] S.A. Ansari, M.H. Cho, Sci. Rep. 7 (2017) 43055.
- [25] D. Zheng, G. Zhang, Y. Hou, X. Wang, Appl. Catal. A 521 (2016) 2–8.
- [26] H. Huang, C. Du, H. Shi, X. Feng, J. Li, Y. Tan, W. Song, Part. Part. Syst. Charact. 32 (2015) 72–79.
- [27] J. Wen, J. Xie, Z. Yang, R. Shen, H. Li, X. Luo, X. Chen, X. Li, A.C.S. Sustain. Chem. Eng. 5 (2017) 2224–2236.
- [28] L. Ge, F. Zuo, J. Liu, Q. Ma, C. Wang, D. Sun, L. Bartels, P. Feng, J. Phys. Chem. C 116 (2012) 13708–13714.
- [29] A. Thomas, A. Fischer, F. Goettmann, M. Antonietti, J.-O. Müller, R. Schlögl, J.M. Carlsson, J. Mater. Chem. 18 (2008) 4893–4908.
- [30] V.N. Khabashesku, J.L. Zimmerman, J.L. Margrave, Chem. Mater. 12 (2000) 3264–3270.
- [31] S. Yan, Z. Li, Z. Zou, Langmuir 25 (2009) 10397–10401.
- [32] X. Jin, X. Fan, J. Tian, R. Cheng, M. Li, L. Zhang, RSC Adv. 6 (2016) 52611–52619.
- [33] J. Duan, S. Chen, M. Jaroniec, S.Z. Qiao, ACS Nano 9 (2015) 931–940.
- [34] J. Wen, X. Li, H. Li, S. Ma, K. He, Y. Xu, Y. Fang, W. Liu, Q. Gao, Appl. Surf. Sci. 358 (2015) 204–212.
- [35] L. Shi, L. Liang, F. Wang, M. Liu, K. Chen, K. Sun, N. Zhang, J. Sun, ACS Sustain. Chem. Eng. 3 (2015) 3412–3419.
- [36] X. Ren, L. Pang, Y. Zhang, X. Ren, H. Fan, S.F. Liu, J. Mater. Chem. A 3 (2015) 10693–10697.
- [37] V. Chikan, D. Kelley, J. Phys. Chem. B 106 (2002) 3794–3804.

[38] W. Ho, J.C. Yu, J. Lin, J. Yu, P. Li, *Langmuir* 20 (2004) 5865–5869.

[39] H. Shi, R. Yan, S. Bertolazzi, J. Brivio, B. Gao, A. Kis, D. Jena, H.G. Xing, L. Huang, *ACS Nano* 7 (2013) 1072–1080.

[40] H. Zhang, W. Tian, L. Zhou, H. Sun, M. Tade, S. Wang, *Appl. Catal. B* 223 (2017) 2–9.

[41] W. Zhao, Y. Liu, Z. Wei, S. Yang, H. He, C. Sun, *Appl. Catal. B* 185 (2016) 242–252.

[42] J. Tong, L. Zhang, F. Li, M. Li, S. Cao, *Phys. Chem. Chem. Phys.* 17 (2015) 23532–23537.

[43] P. Niu, L. Zhang, G. Liu, H.-M. Cheng, *Adv. Funct. Mater.* 22 (2012) 4763–4770.

[44] X. Wang, K. Maeda, A. Thomas, K. Takanabe, G. Xin, J.M. Carlsson, K. Domen, M. Antonietti, *Nat. Mater.* 8 (2009) 76–80.

[45] A.P. Alivisatos, *Science* 271 (1996) 933.

[46] D. Gopalakrishnan, D. Damien, M.M. Shaijumon, *ACS Nano* 8 (2014) 5297–5303.

[47] Y. Wang, Y. Ni, *Anal. Chem.* 86 (2014) 7463–7470.

[48] V. Stengl, J. Henych, *Nanoscale* 5 (2013) 3387–3394.

[49] J.Z. Ou, A.F. Chrimes, Y. Wang, S.-y. Tang, M.S. Strano, K. Kalantar-zadeh, *Nano Lett.* 14 (2014) 857–863.

[50] Y. Hou, A.B. Laursen, J. Zhang, G. Zhang, Y. Zhu, X. Wang, S. Dahl, I. Chorkendorff, *Angew. Chem. Int. Ed.* 52 (2013) 3621–3625.

[51] X. Zong, H. Yan, G. Wu, G. Ma, F. Wen, L. Wang, C. Li, *J. Am. Chem. Soc.* 130 (2008) 7176–7177.

[52] M.A. Lukowski, A.S. Daniel, F. Meng, A. Forticaux, L. Li, S. Jin, *J. Am. Chem. Soc.* 135 (2013) 10274–10277.

[53] Y.-J. Tang, Y. Wang, X.-L. Wang, S.-L. Li, W. Huang, L.-Z. Dong, C.-H. Liu, Y.-F. Li, Y.-Q. Lan, *Adv. Energy Mater.* 6 (2016) 1600116.

[54] J.G. Yu, J. Jin, B. Cheng, M. Jaroniec, *J. Mater. Chem. A* 2 (2014) 3407–3416.

[55] X.P. Xiao, J.H. Wei, Y. Yang, R. Xiong, C.X. Pan, J. Shi, *ACS Sustain. Chem. Eng.* 4 (2016) 3017–3023.

[56] J. Ke, J. Liu, H. Sun, H. Zhang, X. Duan, P. Liang, X. Li, M.O. Tade, S. Liu, S. Wang, *Appl. Catal. B* 200 (2017) 47–55.

[57] K. Shen, X. Xue, X. Wang, X. Hu, H. Tian, W. Zheng, *RSC Adv.* 7 (2017) 23319–23327.

[58] X. Chen, L. Liu, P.Y. Yu, S.S. Mao, *Science* 331 (2011) 746–750.

[59] J. Zhang, X. An, N. Lin, W. Wu, L. Wang, Z. Li, R. Wang, Y. Wang, J. Liu, M. Wu, *Carbon* 100 (2016) 450–455.

[60] Y. Liu, S. Ding, J. Xu, H. Zhang, S. Yang, X. Duan, H. Sun, S. Wang, *Chin. J. Catal.* 38 (2017) 1052–1062.

[61] Y. Liu, J. Xu, L. Wang, H. Zhang, P. Xu, X. Duan, H. Sun, S. Wang, *Nano Sci. Nano Technol. Indian J.* 7 (2017) 64.

[62] M. Li, L. Zhang, X. Fan, M. Wu, Y. Du, M. Wang, Q. Kong, L. Zhang, J. Shi, *Appl. Catal. B* 190 (2016) 36–43.

[63] D. Lu, H. Wang, X. Zhao, K.K. Kondamareddy, J. Ding, C. Li, P. Fang, *ACS Sustain. Chem. Eng.* 5 (2017) 1436–1445.

[64] J.C. Wang, H.C. Yao, Z.Y. Fan, L. Zhang, J.S. Wang, S.Q. Zang, Z.J. Li, *ACS Appl. Mater. Interfaces* 8 (2016) 3765–3775.

[65] P. Zhou, J. Yu, M. Jaroniec, *Adv. Mater.* 26 (2014) 4920–4935.

[66] H. Zhao, Y. Dong, P. Jiang, H. Miao, G. Wang, J. Zhang, *J. Mater. Chem. A* 3 (2015) 7375–7381.